

Large Eddy Simulation of Flows with Complex Moving Boundaries: Application to Flying and Swimming in Animals

Srinivas Ramakrishnan* Lingxiao Zheng† Rajat Mittal‡

Department of Mechanical and Aerospace Engineering

George Washington University, Washington, DC

Fady Najjar§

Lawrence Livermore Laboratory, Livermore, California

George V. Lauder¶

The Museum of Comparative Zoology, Harvard University, Cambridge, MA, USA

and Tyson L. Hedrick||

Department of Biology, University of North Carolina, Chapel Hill, NC-27599

We describe the implementation of a versatile large-eddy simulation (LES) model into an immersed boundary solver and its application to study of swimming and flying in nature. Specifically, we employ the dynamic global coefficient¹ form of the algebraic eddy viscosity model introduced by Vreman.² This model is implemented within a Cartesian grid based IBM amenable to flows with moving boundaries. The implementation is then validated against canonical flows including turbulent channel flow and flow past a circular cylinder. The validated methodology is then applied to the pectoral fin driven yaw turn maneuver of a bluegill sunfish. This flow is typical of biological flows in that the geometry involved are highly complex, three-dimensional and non-stationary and the flow contains laminar, transitional and turbulent zones. The results obtained clearly demonstrate the versatility of the present LES approach for studying complex flows associated with flying and swimming in nature.

I. Introduction

The study of flight and swimming in nature has the potential to significantly improve the design of autonomous systems such as Micro Aerial Vehicles MAVs and Unmanned Underwater Vehicles(UUVs) and computational fluid dynamics is an ideal tool to undertake these studies.³

Figure 1 shows a yaw turn maneuver executed by a bluegill sunfish using just its pectoral fins when viewed from the ventral view (bottom).⁴ These series of images are captured through the use of high-speed and high-resolution cameras.⁴ The freestream is from left to right and a stimulus is introduced from the bottom to induce the turn. In the same figure, we see examples of insect flight showing a butterfly and hawk moth in free flight. Note the complex motion and deformation i.e. kinematics of the fins/wings that these animals exhibit in their locomotion. Clearly, the study of such flows requires sophisticated computational tools that can handle complicated geometries undergoing general motion.

*Postdoctoral Scientist, AIAA Member

†Ph.D. Student, AIAA Student Member

‡Professor, AIAA Senior Member.

§Code Physicist, AIAA Senior Member

¶Professor.

||Professor

Here, a Cartesian grid immersed boundary method (IBM) is particularly attractive due its inherent capabilities to accommodate complex moving boundaries.⁵⁻⁷ The results⁸ obtained by applying our IBM for the flows described above are shown in Figure 2. Through the flexibility of its pectoral fins, the sunfish successfully produces a vortex ring-like structure that supplies the impulse force for executing the yaw turn⁸(refer to the performance coefficients for the maneuver shown in Figure 2). Meanwhile, the moth⁹ relies on a series of complex interactions of wing tip vortices, shown in Figure 2, to sustain lift to balance its own weight during hover. Figure 2 also shows the time variation of the lift forces generated by the moth. Clearly, both these flows are dominated by highly transient vortex dynamics that generate highly time dependent force responses.^{8,9}

Thus, high fidelity methods, that adequately capture these important dynamical structures, are essential for any meaningful study of such flows. However, while direct numerical simulation (DNS) can be used for low Reynolds numbers situations, many configuration of practical interest have Reynolds numbers that are not amenable to DNS. Therefore, to extend these studies to higher Reynolds numbers, a systematic strategy to improve computational efficiency without sacrificing accuracy and fidelity needs to be developed. Large Eddy Simulation (LES) methodology, an intermediate between DNS and RANS, offers the ideal balance of computational efficiency and accuracy. While there are a number of LES models in existence, few meet the practical requirements for successfully simulating non-equilibrium, inhomogeneous flows that simultaneously contain laminar, transitional and turbulent regimes that are commonly encountered in flows of interest. For example, the attached boundary layer on the body of the sunfish due to incoming freestream is laminar and the action of the pectoral fin can potentially cause the wake to quickly transition to turbulence.

A subgrid scale model is needed that not only exhibits the correct response to laminar and turbulent regions but can also function in highly inhomogeneous flow with complex moving boundaries. These requirements eliminate most of the well-known SGS models in use today. The recently developed the global coefficient model^{1,2} is the only one that seems to have the requisite properties and we describe the implementation, validation and use of this mode within a Cartesian grid immersed boundary method.⁷

This paper is organized as follows. Section 2 describes the immersed boundary methodology employed including details of the SGS model implementation. Sections 3, and 4 discuss validation of our model implementation using a turbulent channel and cylinder in cross flow, respectively. Section 5 demonstrates the capabilities of the validated framework using a bluegill sunfish yaw turn maneuver. Finally, we end with a summary of our accomplishments and future goals.

II. Methodology

A. Computational Methodology

We present a brief description of the Cartesian grid based immersed boundary method for moving boundaries starting with the governing equations. Further details can be found in Mittal et al. (2008). The three-dimensional unsteady, viscous incompressible Navier-Stokes equations are given as

$$\frac{\partial u_i}{\partial x_i} = 0 \quad (1)$$

$$\frac{\partial u_i}{\partial t} + \frac{\partial(u_i u_j)}{\partial x_j} = -\frac{1}{\rho} \frac{\partial p}{\partial x_i} + \nu \frac{\partial}{\partial x_j} \left(\frac{\partial u_i}{\partial x_j} \right) \quad (2)$$

where $i, j = 1, 2, 3$, u_i are the velocity components, p is the pressure, and ρ and ν are the fluid density, kinematic viscosity.

1. Numerical Method

The Navier-Stokes equations (9) are discretized using a cell-centered, collocated (non-staggered) arrangement of the primitive variables (u_i, p). In addition to the cell-center velocities (u_i), the face-center velocities, U_i , are computed. A second-order Adams-Bashforth scheme is employed for the convective terms while the diffusion terms are discretized using an implicit Crank-Nicolson scheme which eliminates the viscous stability constraint. The

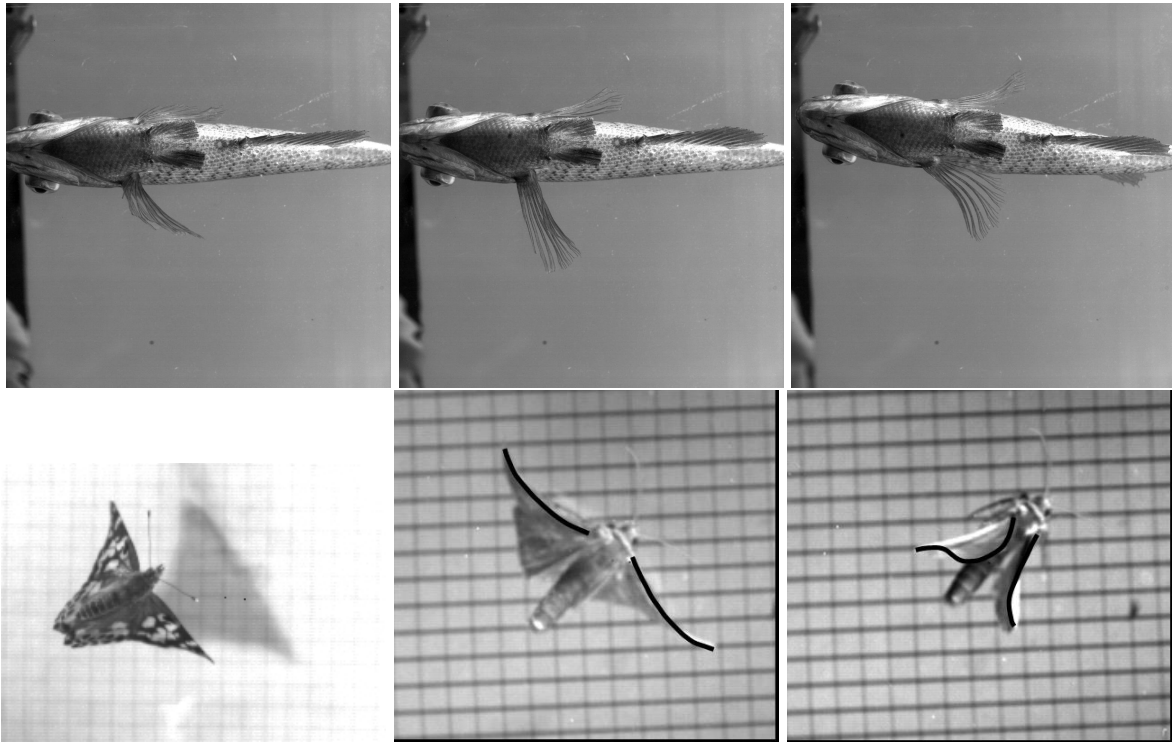


Figure 1. (Top) A bluegill sunfish during a maneuver from a ventral view, the fin extending out into the flow is the referred to as the strongside fin; (Bottom) Butterfly (leftmost) and moth in free flight

spatial derivatives are computed using a second-order accurate central difference scheme. The equations are integrated in time using the fractional step method.¹⁰ In the first sub-step of this method, a modified momentum equation is solved and an intermediate velocity u^* obtained. The second sub-step requires the solution of the pressure correction equation which is solved with the constraint that the final velocity u_i^{n+1} be divergence-free. A Neumann boundary condition is imposed on this equation at all boundaries and the equation is solved with a highly efficient geometric multigrid method which employs a Gauss-Siedel line-SOR smoother. Once the pressure correction is obtained, the pressure and velocity are updated. These separately updated face-velocities satisfy discrete mass-conservation to machine accuracy and use of these velocities in estimating the non-linear convective flux leads to a more accurate and robust solution procedure. The advantage of separately computing the face-center velocities was initially proposed by Zang et al.¹¹ and discussed in the context of the Cartesian grid methods in Ye et al.¹²

2. Immersed Boundary Treatment

The immersed boundary method described here employs a multi-dimensional ghost-cell methodology to impose the boundary conditions on the immersed boundary. The current solver is designed from the start for fast, efficient and accurate solution of flows with complex *three-dimensional, moving* boundaries. Also, the current method is a “sharp” interface method in that the boundary conditions on the immersed boundary are imposed at the precise location of the immersed body and there is no spurious spreading of boundary forcing into the fluid as what usually occurs with diffuse interface methods (See Mittal & Iaccarino⁵ for details).

3. Geometric Representation of Immersed Boundary

The current method is designed to simulate flows over arbitrarily complex 2D and 3D immersed stationary and moving boundaries and the approach chosen to represent the boundary surface should be flexible enough so as not to limit the type of geometries that can be handled. In the current solver we choose to represent the surface of the IB by

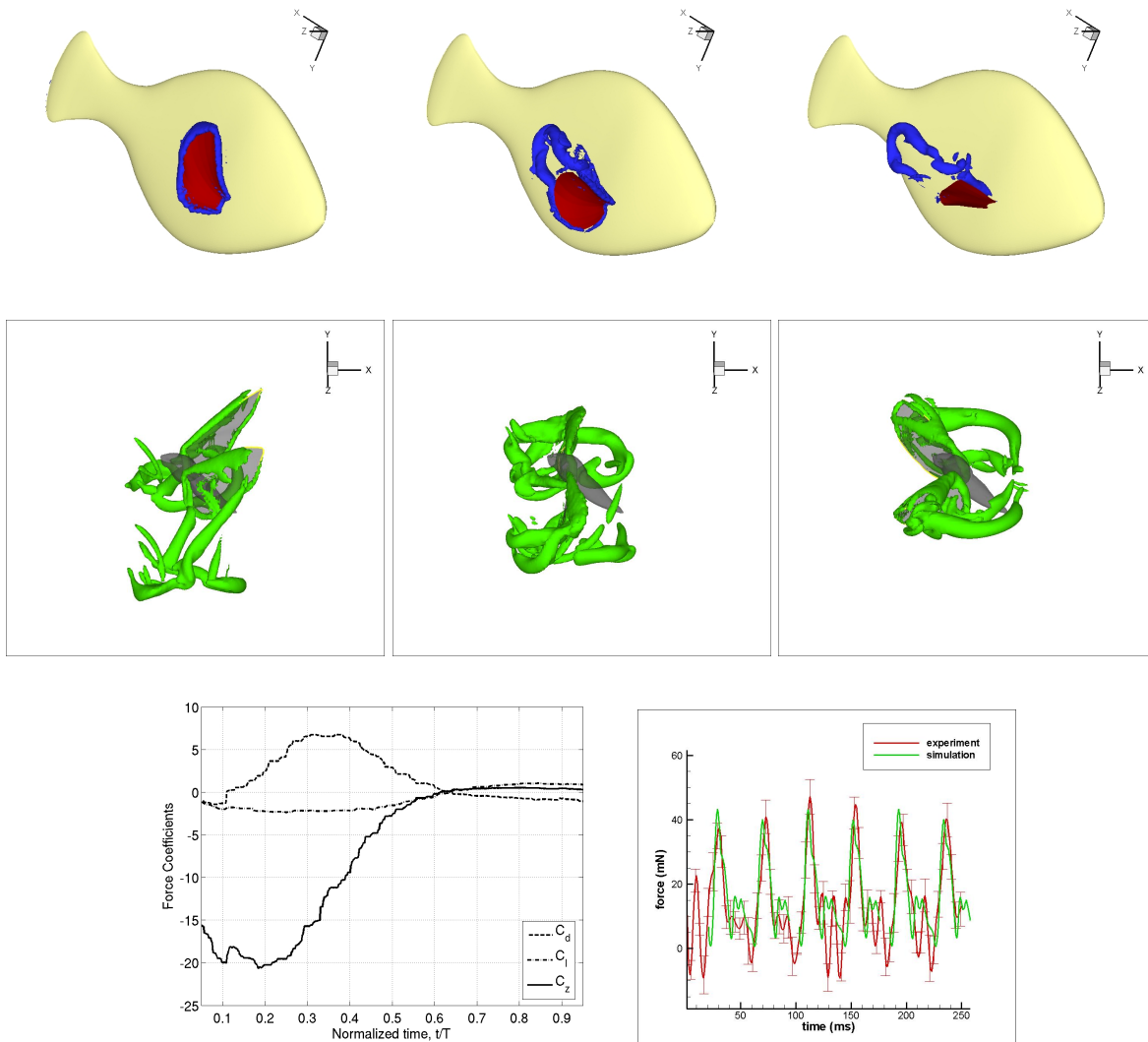


Figure 2. Formation of the vortex ring due to the strongside pectoral fin motion (First row). The vortex structures during a hawkmoth hover (Second row). The associated performance coefficients for maneuvering bluegill sunfish (left) and hovering hawk moth (right) (Third row). All the results obtained without any SGS models.

a unstructured mesh with triangular elements. This approach is very well suited for the wide variety of flow engineering and biological configurations that we are interested and is compatible with the immersed boundary methodology used in the current solver.

4. Ghost-Cell Formulation

First, the surface mesh (see Figure 3) is embedded or immersed into the Cartesian grid. Next, a systematic procedure is developed to implement the ghost-cell methodology for such an immersed boundary. The method begins with identifying cells whose nodes are inside the solid boundary (termed “solid cells”) and cells that are outside the body (termed “fluid cells”). Once the solid-fluid interface has been determined, the next step is to mark the so-called “ghost-cells”. These are cells whose nodes are inside the solid but which have at least one north, south, east or west neighbor in the fluid. The overall approach now is to determine an appropriate equation for these ghost cells that implicitly satisfies the imposed physical boundary condition on the immersed boundary in the vicinity of each ghost-cell. This is accomplished by extending a line segment from the node of these cells into the fluid to an “image-point” (denoted by IP) such that it intersects normal to the



Figure 3. Schematic describing naming convention and location of velocity components (left) and the ghost-cell method (right).

immersed boundary and the boundary intercept (denoted by BI) lies midway between the ghost-node and the image-point. Next, the cells surrounding the IP are identified and bilinear interpolation is used to compute the value of generic variable ϕ at the image point as follows,

$$\phi_{IP} = \sum \beta_i \phi_i \quad (3)$$

where i extends over all the surrounding cells and β_i are the associated interpolation weights of these cells. Following this, the value of the variable at the ghost-cell (denoted by GC) is computed by using a central-difference approximation along the normal probe which incorporates the prescribed boundary condition at the boundary intercept. Thus, for Dirichlet and Neumann boundary conditions, the formulas are:

$$\phi_{GC} = 2\phi_{BI} - \phi_{IP} \quad (4)$$

and

$$\phi_{GC} = \Delta l_p \left(\frac{\delta \phi}{\delta n} \right)_{BI} + \phi_{IP} \quad (5)$$

respectively where Δl_p is the total length of the normal line segment. Equations 4 and 5 can now be combined with Eq. 3 to give an implicit expression for the ghost-node values ie.

$$\phi_{GC} + \sum \beta_i \phi_i = 2\phi_{BI} \quad (6)$$

and

$$\phi_{GC} - \sum \beta_i \phi_i = \Delta l_p \left(\frac{\delta \phi}{\delta n} \right)_{BI} \quad (7)$$

respectively for these two types of boundary conditions. These equations are then solved in a fully coupled manner with the discretized governing equations 2 for the neighboring fluid cells along with the trivial equation $\phi = 0$ for the internal solid cells. Using this procedure, the boundary conditions are prescribed to second-order accuracy, and this along with the second-order accurate discretization of the fluid cells, leads to local and global second-order accuracy in the computations.

5. Large Eddy Simulation

As discussed earlier, we introduce subgrid scale (SGS) modeling to enable the present IBM framework to tackle higher Reynolds number in a computationally efficient manner.

A formal introduction of LES begins with an application of a grid level filter to Equation 2 to obtain the filtered equations of motion.

$$\frac{\partial \bar{u}_i}{\partial x_i} = 0 \quad (8)$$

$$\frac{\partial \bar{u}_i}{\partial t} + \frac{\partial(\bar{u}_i \bar{u}_j)}{\partial x_j} = -\frac{1}{\rho} \frac{\partial \bar{p}}{\partial x_i} + \nu \frac{\partial}{\partial x_j} \left(\frac{\partial \bar{u}_i}{\partial x_j} \right) - \frac{\partial \tau_{ij}}{\partial x_j} \quad (9)$$

where τ_{ij} is the subgrid scale stress tensor. This term is modeled through an eddy viscosity approach such that

$$\tau_{ij} - \frac{1}{3} \delta_{ij} \tau_{ij} = -2\nu_e \bar{S}_{ij} \quad (10)$$

where $\bar{S}_{ij} = \frac{1}{2} \left(\frac{\partial \bar{u}_i}{\partial x_j} + \frac{\partial \bar{u}_j}{\partial x_i} \right)$ is the strain-rate tensor and ν_e is the eddy viscosity.

There are several SGS models in existence that may be used to construct the eddy viscosity in equation 10. The simplest SGS model is the Smagorinsky model,¹³ but the need for *ad-hoc* wall damping¹⁴ to limit spurious dissipation in the near-wall region makes it unsuitable as a candidate for use in complex inhomogeneous flows. Next, there is the extensively used dynamic Smagorinsky model¹⁵ which exhibits the correct near-wall behavior, but requires at least one homogeneous direction for its dynamic procedure to be successful. Meanwhile, the dynamic Lagrangian model eliminates the restrictions on homogeneity by averaging along pathlines making it suitable for use in general flows.¹⁶ However, the selection of model parameters related time scale (needed for the dynamic procedure) in highly transient vortex dominated flows is not straightforward.¹⁶

Here we explore a new gradient based subgrid scale model, introduced by Vreman,² that is well suited for these types of complex flows. The original model introduced by Vreman² is formulated as follows:

$$\nu_e = C_\nu \Pi^g, \quad (11)$$

where C_ν is the global coefficient. Furthermore,

$$\Pi^g = \sqrt{\frac{B_\beta^g}{\bar{\alpha}_{ij} \bar{\alpha}_{ij}}}, \quad (12)$$

$$B_\beta^g = \beta_{11}^g \beta_{22}^g - \beta_{12}^g \beta_{12}^g + \beta_{11}^g \beta_{33}^g - \beta_{13}^g \beta_{13}^g + \beta_{22}^g \beta_{33}^g - \beta_{23}^g \beta_{23}^g, \quad (13)$$

$$\beta_{ij}^g = \sum_{m=1}^3 \bar{\Delta}_m^2 \bar{\alpha}_{mi} \bar{\alpha}_{mj}, \quad (14)$$

and

$$\bar{\alpha}_{ij} = \frac{\partial \bar{u}_j}{\partial x_i} \quad (15)$$

The superscript g denotes the grid filter associated with the grid level length scale $\bar{\Delta}$.

A method for dynamically updating the Vreman model coefficient was introduced first by Park et al¹⁷ based on a two-level test filtering approach. Recently, You and Moin¹ derived a dynamic procedure for the Vreman model that requires only single test filter. This dynamic procedure does not rely on spatial and temporal averaging and is therefore very well suited for complex inhomogeneous flows. A detailed discussion of this dynamic procedure is presented in You and Moin.¹ The current implementation of the dynamic procedure follows that of You and Moin.¹ For brevity, we present just the final expression for the coefficient.

$$C_\nu = -\frac{\nu}{2} \frac{\langle \widehat{\bar{\alpha}_{ij} \bar{\alpha}_{ij}} - \hat{\bar{\alpha}}_{ij} \hat{\bar{\alpha}}_{ij} \rangle}{\langle \Pi^g \widehat{\bar{S}_{ij} \bar{S}_{ij}} - \Pi^t \hat{\bar{S}}_{ij} \hat{\bar{S}}_{ij} \rangle} \quad (16)$$

The superscript t and $\hat{\cdot}$ are associated with the test level filter operation that use a length scale $\hat{\Delta} = 2\bar{\Delta}$. The filter employed here is the spherical box filter. And, $\langle \cdot \rangle$ denote a volume average over the entire domain. This model is hereafter referred to as the dynamic Vreman model.

The ghost cell methodology (refer to section 4) based IBM affords a consistent manner in which to implement the SGS model. To elaborate, the ghost cell values are employed in both the test filtering operation and velocity gradient evaluation at the cells adjacent to the immersed boundaries in the fluid domain.

III. Validation - Turbulent Channel Flow at $Re_\tau = 395$

Re_τ	L_x	L_y	L_z	N_x	N_y	N_z	Δx^+	Δz^+	Δy_w^+
395	$2\pi\delta$	2δ	$\frac{2\pi\delta}{3}$	48	64	48	48	18	0.95

Table 1. Simulation parameters for the turbulent channel flow.

We now test the Vreman model implementation using the canonical planar turbulent channel flow for which reference data is readily available.¹⁸ The simulation parameters for the channel are summarized in Table 1. Turbulence statistics, obtained using the current IBM framework, for a fixed coefficient Smagorinsky model with wall damping, fixed coefficient Vreman model,² and the dynamic Vreman model¹ are compared with the reference DNS¹⁸ in Figure 4. The fixed coefficient for Vreman and Smagorinsky model are $C_\nu = 0.07^2$ and $C_s = 0.1$, respectively. The fixed coefficient Vreman model produces results of similar quality as the Smagorinsky model with wall damping. Now, the introduction of the global dynamic procedure (see Equation 16) for the model coefficient noticeably improves the solution (refer to Figure 4). This improvement is seen most clearly in the spanwise turbulence intensity plot. The time history of the model coefficient computed using Equation 16 is nearly identical to that reported in You and Moin¹ (see Figure 5). The mean value for the dynamic global coefficient, C_ν is 0.05. The differences in the low order statistics between the fixed and dynamic Vreman model, shown in Figure 4, are consistent with the coefficients employed. Finally, a plot of instantaneous normalized velocity and eddy viscosity in Figure 5 clearly shows that the model shows the correct behavior as we approach the wall *without an explicit wall model*. Overall, the quality of results obtained with our implementation is comparable to those reported by Vreman² and You and Moin.¹

The elimination of the need for wall damping and a dynamic procedure that is not reliant on homogeneous directions makes the extension of the present framework to complex geometries straightforward. We now describe the results of simulations with more complex immersed boundaries.

IV. Cylinder in Crossflow at $Re=1000$

Re_d	L_x	L_y	L_z	N_x	N_y	N_z
1000	40	40	π	256	144	32

Model	C_d
No Model	1.04
Dynamic Vreman	1.04

Table 2. Simulation parameters for the cylinder and time averaged drag coefficients.

The simulations parameter for cylinder are summarized in Table 2. The primary purpose of this test case is to evaluate the performance of the SGS model in the presence of an immersed body. We plan to perform a more rigorous quantitative comparison against the widely used $Re = 3900$ case in the future.

Figure 6 shows the time history of the drag coefficients for the no-model, and dynamic coefficient Vreman model. Here, both cases are in relatively good agreement with the established experimental value close to unity¹⁹ (refer to Table 2). The cylinder wake structure, shown in figure 7, at this Reynolds exhibits the characteristic three dimensional braid like structures.

The contours of the eddy viscosity normalized by the physical viscosity highlight where

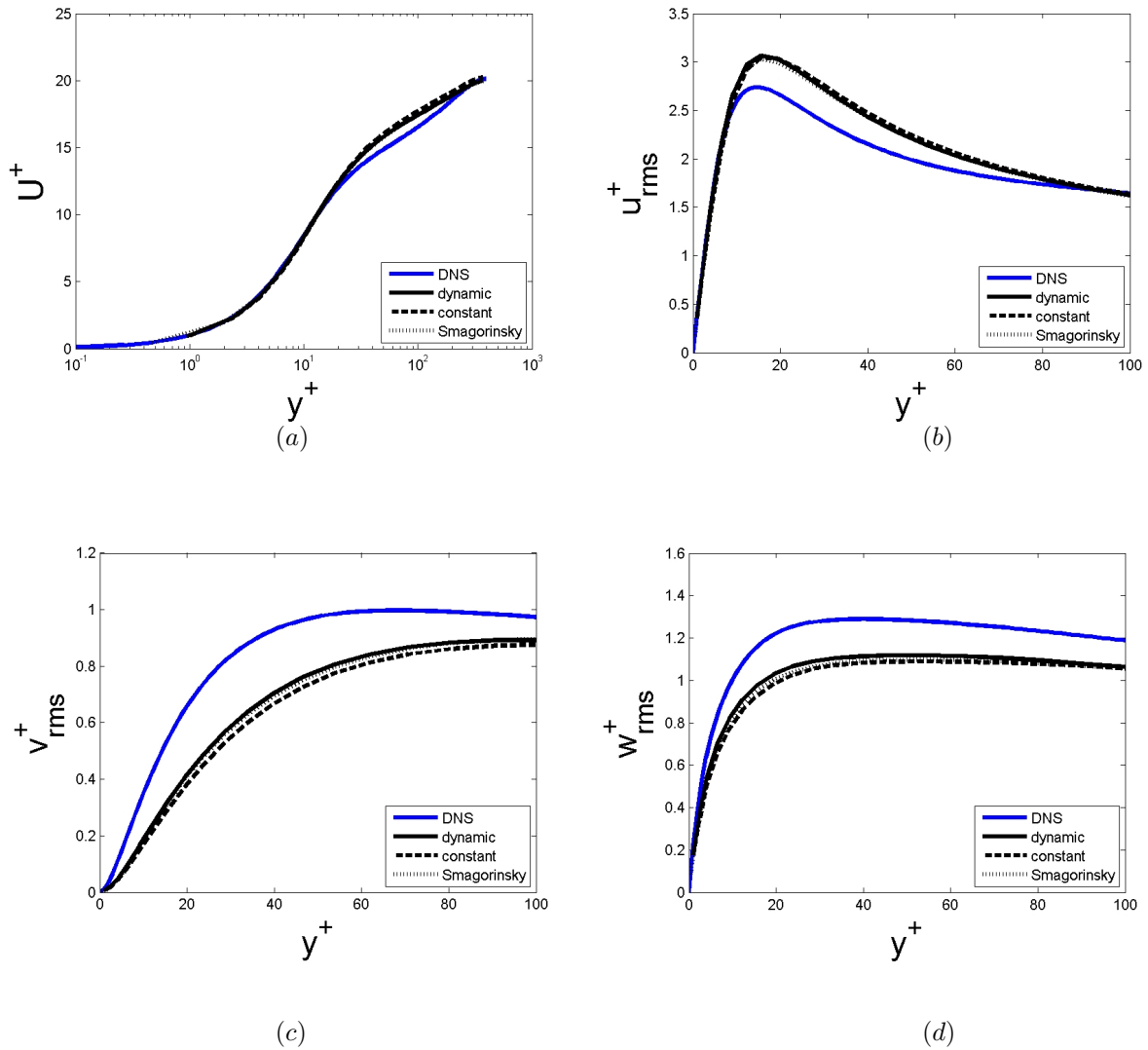


Figure 4. Turbulent channel flow statistics for different models: blue solid line - DNS; solid - Dynamic Vreman; dashed - Constant coefficient Vreman; dotted Smagorinsky with wall damping

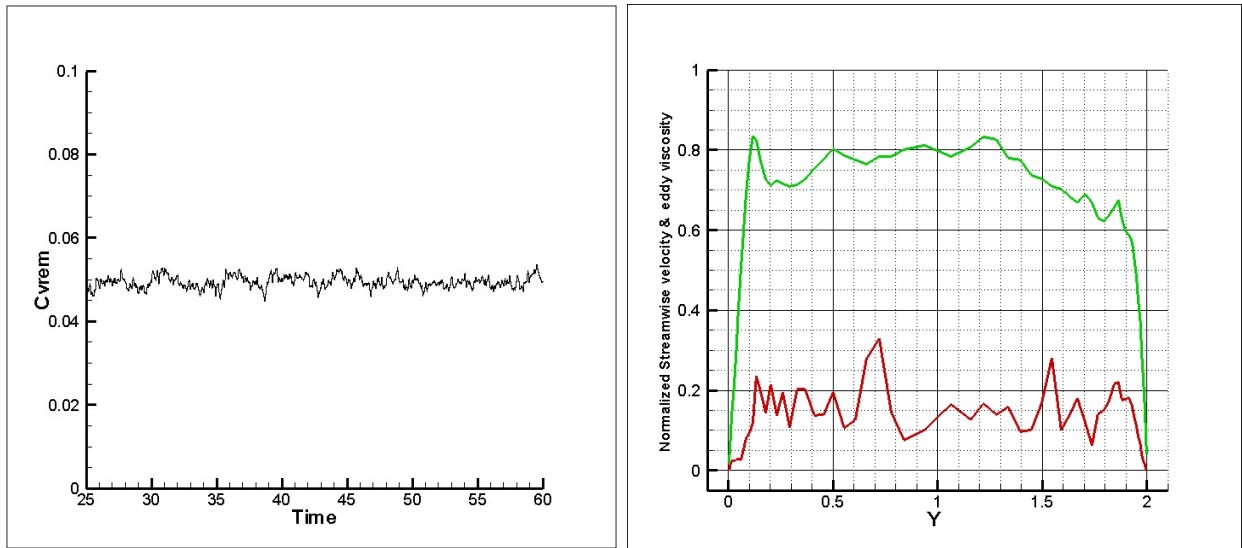


Figure 5. Time history of the global dynamic coefficient for the turbulent channel flow(left). Profiles of instantaneous streamwise velocity normalized by maximum velocity(green) and eddy viscosity normalized by molecular viscosity (red) for the turbulent channel flow (right).

the SGS models are most active(refer to Figures 8). The eddy viscosity introduced is on the order of physical viscosity and the peak normalized value is close to 2.0. Note however that the value for a large portion of the wake, where the model is active, nominally ranges between to 0.5 to 1.0 (see Figure 8).

Significantly, the dynamic Vreman model is successful in introducing eddy viscosity strictly in the areas where the flow is expected to be turbulent i.e. in the cylinder wake. Additionally, the eddy viscosity contribution in the attached boundary layer is minimal. This is encouraging since the excessive viscosity introduced by the subgrid scale may interfere with proper evolution of the dynamical structures in the flow.

V. Bluegill Sunfish Yaw Maneuver

Finally, we explore the ability of the LES modeling developed here for our target application - moving boundary problems encountered in biological flows. Experimental⁴ and numerical investigations⁸ have clearly shown that the primary thrust for the yaw turn maneuver of the bluegill sunfish is derived from the strongside pectoral fin (see Figure 1). Therefore, in the context of studying the SGS model performance, we focus just on the strongside pectoral fin hydrodynamics. The strong side pectoral fin during a maneuver

Re_d	L_x	L_y	L_z	N_x	N_y	N_z
1200	22	20	20	160	128	128

Table 3. Simulation parameters for the Bluegill Sunfish .

is shown in Figure 9. The fin is modeled as a deforming membrane with zero thickness. The simulation parameters are summarized in Table 3. The Reynolds number is defined as $Re = U_\infty L_s / \nu$, where U_∞ , L_s , and ν are the fish forward velocity, spanwise fin length, and the kinematic viscosity of water ($\nu = 1.007 \times 10^{-6} m^2 s^{-1}$ at room temperature (20 degrees Celsius)). The experimental Reynolds number for the turning maneuver is approximately 3500 based on spanwise fin length and a turning velocity of 0.5 body lengths per second. For preliminary LES model performance evaluation, we are employing a Reynolds number that is approximately a third of the experimental value. The boundary conditions on the domain are freestream on the right hand side, outflow on the left while the remaining boundaries employ slip or symmetry boundary conditions (see Figure 9). Finally, the fin

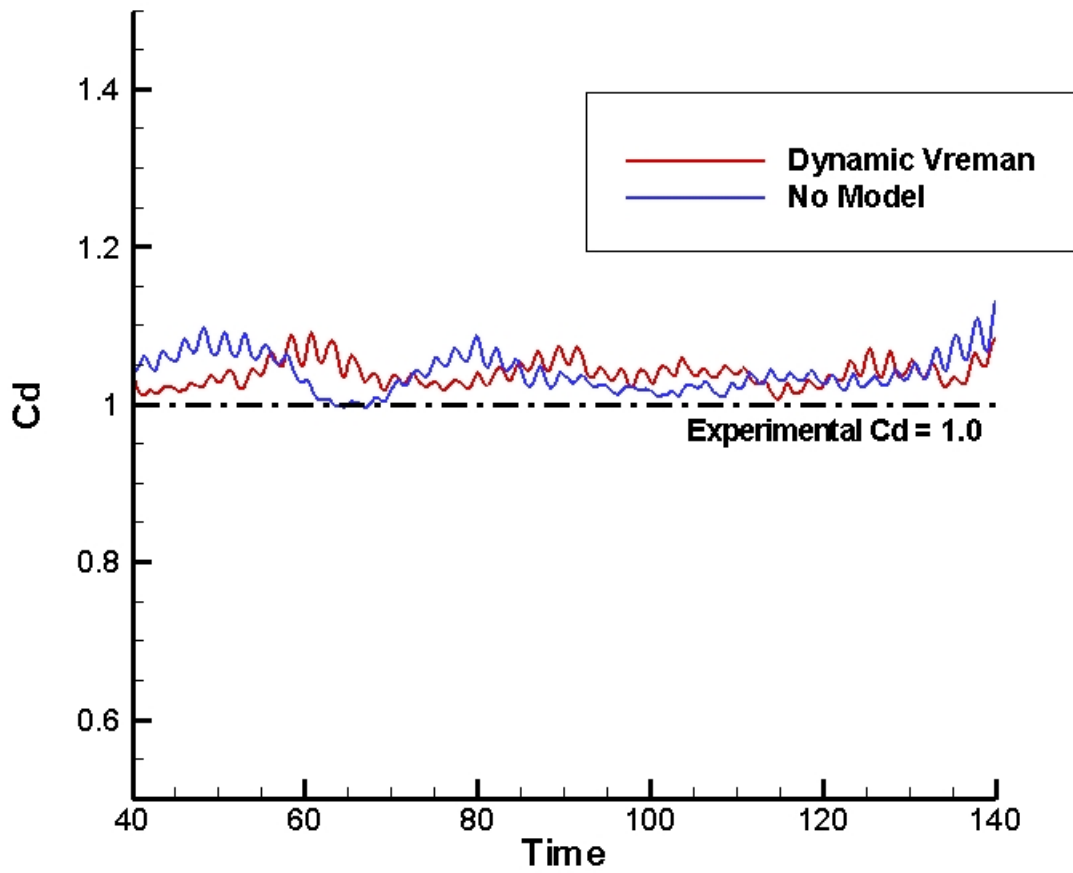


Figure 6. The time history of the drag coefficient with different SGS models.



Figure 7. The wake structure of the cylinder.

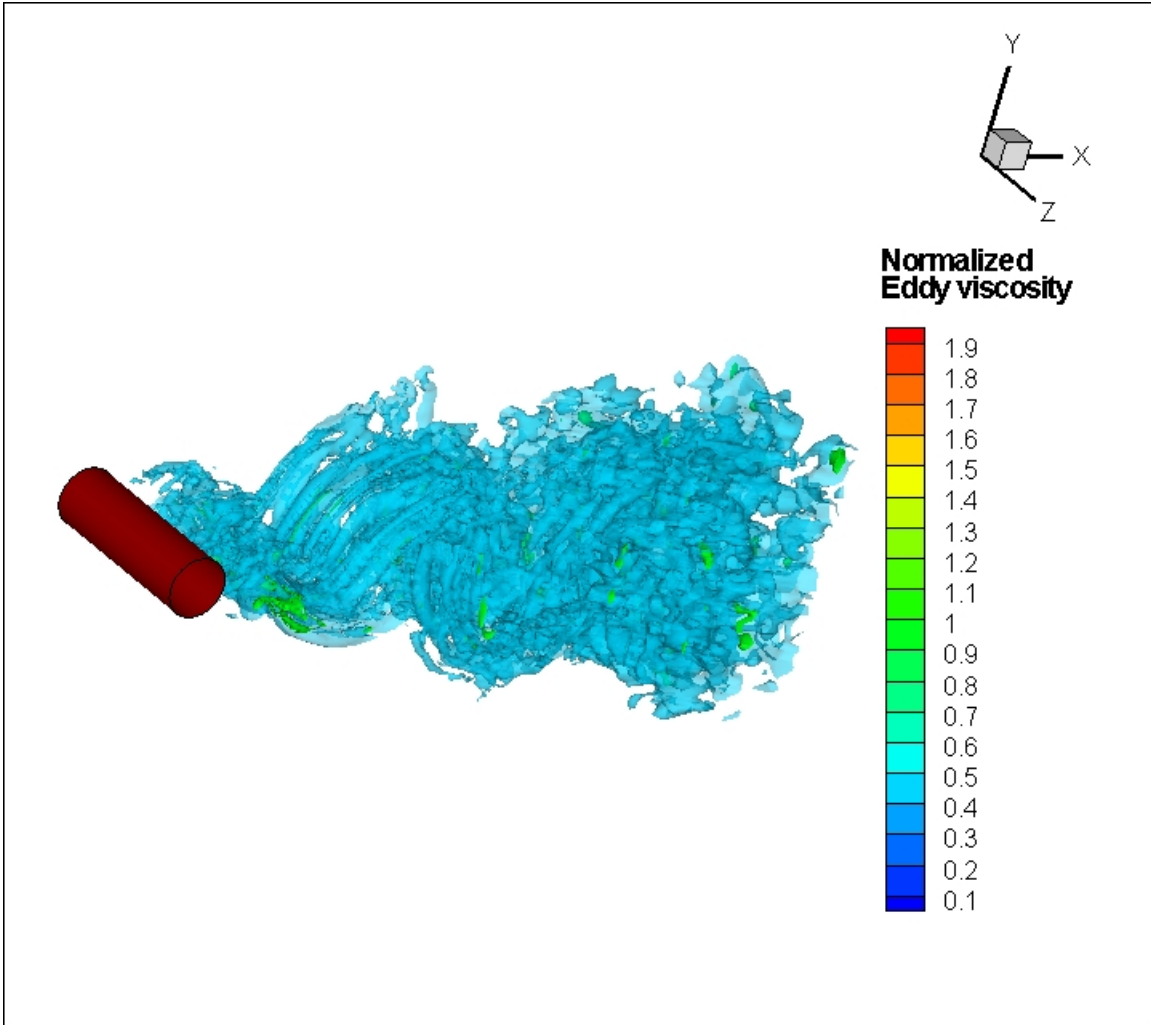


Figure 8. An instantaneous normalized eddy viscosity distribution for dynamic Vreman model. The eddy viscosity is normalized by the physical viscosity

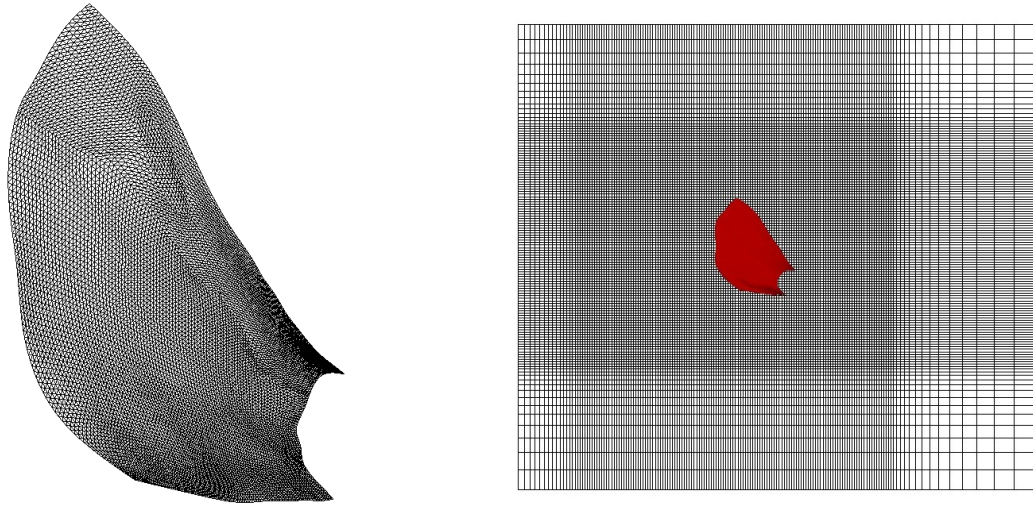


Figure 9. Strongside fin setup used in the yaw turn maneuvering. Unstructured surface mesh with 8281 nodes and 16200 triangular elements (Left). The fin embedded in the Cartesian grid (right).

surface is considered a no slip boundary.

The vortex ring like structure observed in the experiments and past computations^{4,8} is preserved even when LES model is activated (see Figure 10). This suggests that the Vreman model does not introduce excessive dissipation that may adversely affect the important vortex dynamics governing such flows. Figure 11 shows the time history of normalized forces developed on the strongside fin. The forces are normalized using the maximum value of the lateral (C_z) force. The forces predicted are similar to that obtained with the no model case⁸ (refer to Figure 2).

Similar to the cylinder case, we examine the distribution of eddy viscosity at a particular instant (see Figure 12). The wake flow structures are also overlaid on the same plot. The near perfect correlation of the eddy viscosity distribution with the vortical structure (refer to Figure 12) illustrates the efficacy of the modeling in targeting regions of the flow that are turbulent. It is noteworthy that this important feature is preserved even for a flow with complex geometries undergoing non-trivial motion. Thus, establishing the robustness of the LES methodology implemented here for studying such flows.

VI. Conclusions

A global dynamic coefficient large-eddy simulation modeling approach suitable for studying biological locomotion has been implemented in an existing immersed boundary solver. The versatility of this overall approach is demonstrated for a complex case associated with pectoral fin hydrodynamics. Initial results are encouraging and future work will focus on exploring higher Reynolds number flows as well as flows associated with insect flight.⁹

VII. Acknowledgments

This work is supported under ONR-MURI Grant N00014-03-1-0897 and NSF grant CBET-0828147.

References

- ¹You, D. and Moin, P., “A Dynamic Global-coefficient Subgrid-scale Eddy Viscosity Model for Large Eddy Simulation in Complex Geometries,” *Physics of Fluids*, Vol. 19, 2007, pp. 065110–1–065110–8.
- ²Vreman, A., “An Eddy Viscosity Subgrid-scale Model for Turbulent Shear Flow: Algebraic Theory and Applications,” *Physics of Fluids*, Vol. 16, 2004, pp. 3670–3680.
- ³Mittal, R., “Computational Modeling in Biohydrodynamics: Trends, Challenges, and Recent Advances,” *IEEE J. Oceanic Eng.*, Vol. 29, No. 3, 2004, pp. 595–604.

- ⁴Drucker, E. G. and Lauder, G. V., “Wake Dynamics and Fluid Forces of Turning Maneuvers in Sunfish,” *J. Exp. Biol.*, Vol. 204, 2001, pp. 431–442.
- ⁵Mittal, R. and Iaccarino, G., “Immersed Boundary Methods,” *Annu. Rev. Fluid Mech.*, Vol. 37, 2005, pp. 239–61.
- ⁶Dong, H., Mittal, R., and Najjar, F. M., “Wake Topology and Hydrodynamic Performance of Low-aspect-ratio Flapping Foils,” *J. Fluid Mech.*, Vol. 566, 2006, pp. 309–343.
- ⁷Mittal, R., Dong, H., Bozkurttas, M., Najjar, F. M., Vargas, A., and Loebbecke, A. V., “A Versatile Sharp Interface Boundary Method for Incompressible Flows with Complex Boundaries,” *J. Comp. Phys.*, Vol. 227, 2008.
- ⁸Ramakrishnan, S., Mittal, R., Lauder, G., and Bozkurttas, M., “Analysis of Maneuvering Fish Fin Hydrodynamics Using an Immersed Boundary Method,” *38th AIAA Fluid Dynamics Conference and Exhibit*, Seattle, Washington, 2008.
- ⁹Zheng, L., Wang, X., Khan, A., Vallance, R. R., Mittal, R., and Hedrick, T. L., “A Combined Experimental-Numerical Study of the Role of Wing Flexibility in Insect Flight,” *47th AIAA Aerospace Sciences Meeting Including The New Horizons Forum and Aerospace Exposition*, Orlando, Florida, 2009.
- ¹⁰Chorin, A. J., “A Numerical Method for Solving Incompressible Viscous Flow Problems,” *J. Comp. Phys.*, Vol. 2, 1967.
- ¹¹Zang, Y., Streett, R. L., and Koseff, J. R., “A Non-Staggered Fractional Step Method for Time-Dependent Incompressible Navier-Stokes Equations in Curvilinear Coordinates,” *J. Comp. Phys.*, Vol. 114, 1994, pp. 18–33.
- ¹²Ye, T., Mittal, R., Udaykumar, H. S., and Shyy, W., “An accurate Cartesian grid method for simulation of viscous incompressible flows with complex immersed boundaries,” *J. Comput. Phys.*, Vol. 156, 1999, pp. 209–240.
- ¹³Smagorinsky, J., “General Circulation Experiments with Primitive Equations,” *Mon. Weather Rev.*, Vol. 91, 1963.
- ¹⁴Driest, E. V., “On Turbulent Flow Near a Wall,” *Journal of Aerospace Science*, Vol. 23, 1956.
- ¹⁵Smagorinsky, J., “A Dynamic Subgrid Scale Eddy-Viscosity Model,” *Physics of Fluids A*, Vol. 3, 1991, pp. 1760.
- ¹⁶Meneveau, C., Lund, T., and Cabot, W., “A Lagrangian Dynamic Subgrid Scale Model of Turbulence,” *Journal of Fluid Mechanics*, Vol. 319, 1996, pp. 353–385.
- ¹⁷Park, N., Lee, S., Lee, J., and Choi, H., “A Dynamic Subgrid-scale Eddy Viscosity Model with a Global Coefficient,” *Physics of Fluids*, Vol. 18, 2006, pp. 125109–1–125109–24.
- ¹⁸Moser, R., Kim, J., and Mansour, N., “Direct Numerical Simulation of turbulent channel flow up to $Re_\tau = 590$,” *Physics of Fluids*, Vol. 11, 1999, pp. 943–945.
- ¹⁹Wieselsberger, C., “New data on the laws of fluid resistance,” *NACA Technical Note 84*, 1922.

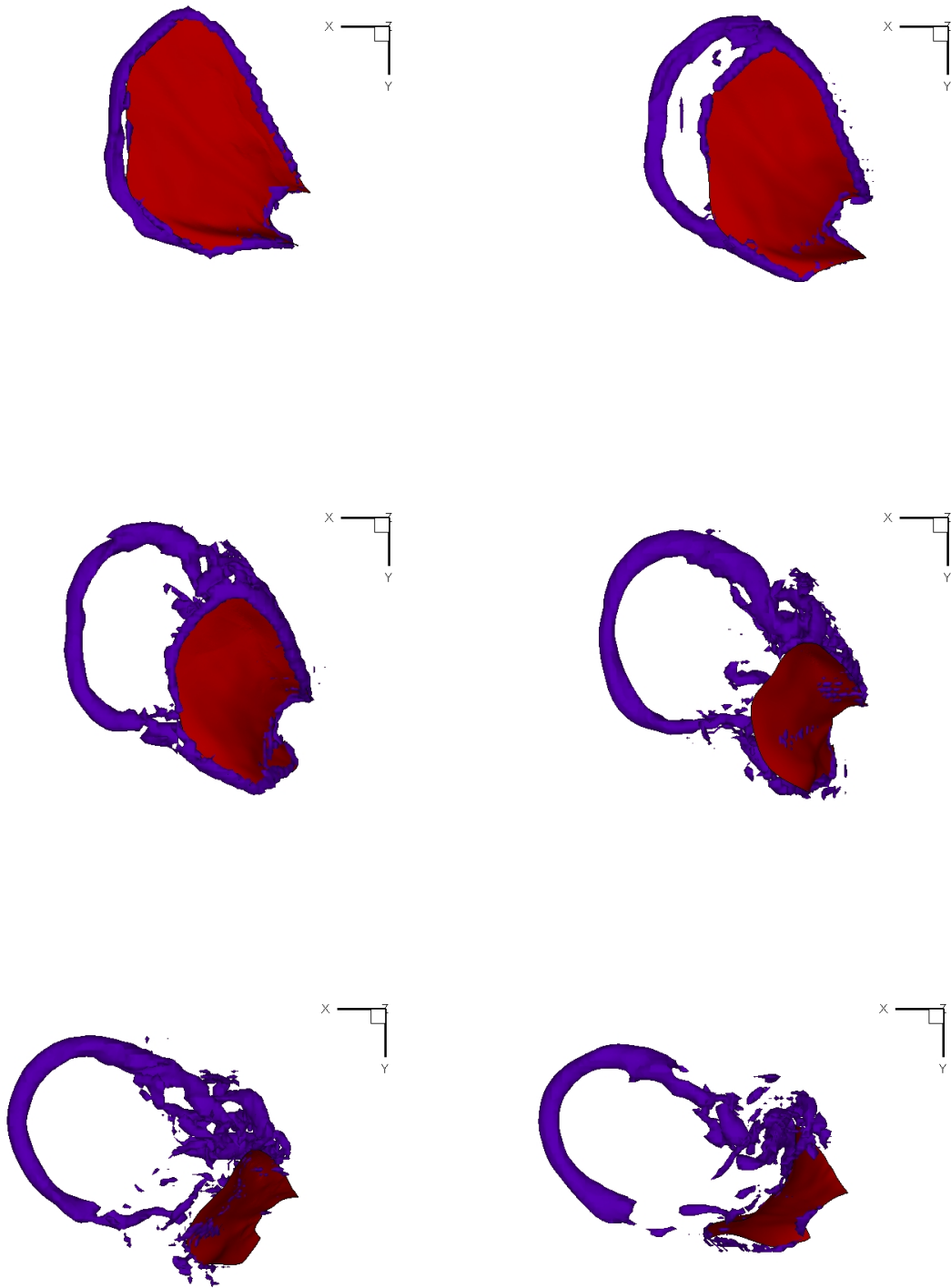


Figure 10. Formation of the vortex ring due to the strongside pectoral fin motion. $t/T = 0.12$ and $t/T = 0.25$ (first row). $t/T = 0.37$ and $t/T = 0.50$ (second row). $t/T = 0.62$ and $t/T = 0.75$ (third row).

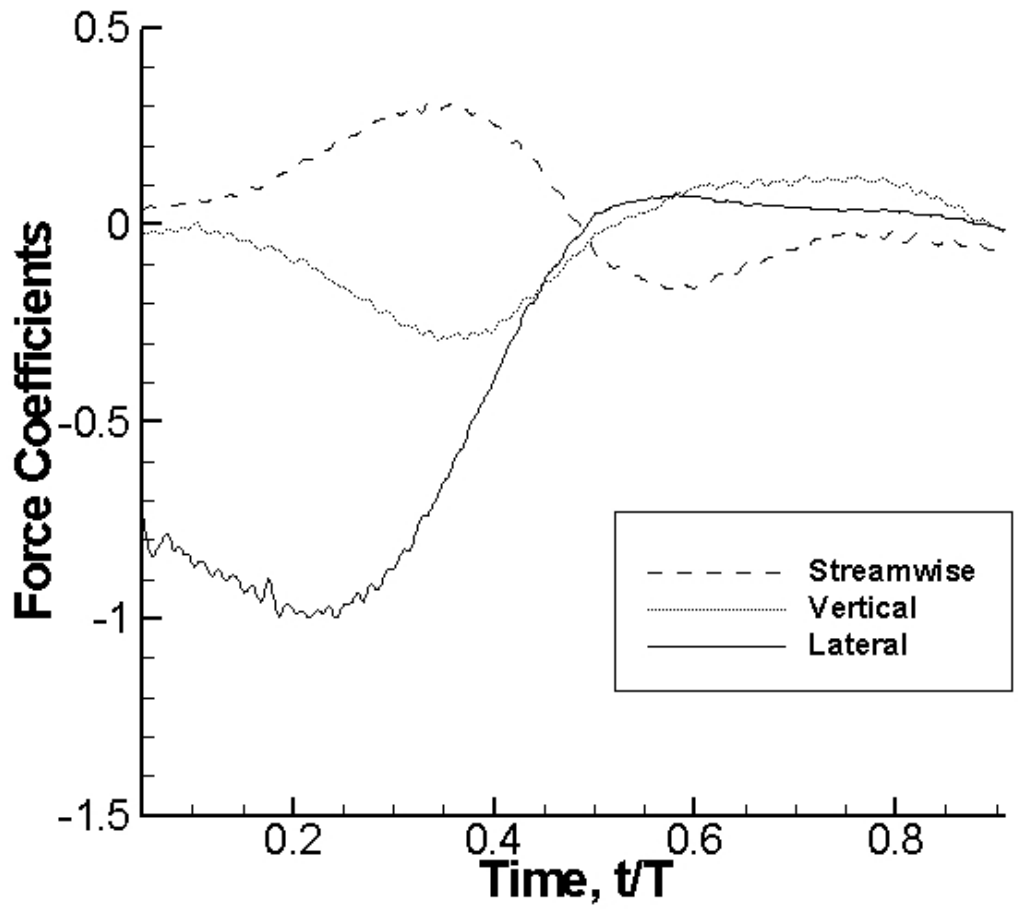


Figure 11. Normalized force coefficients force history for the strongside fin using the dynamic Vreman model

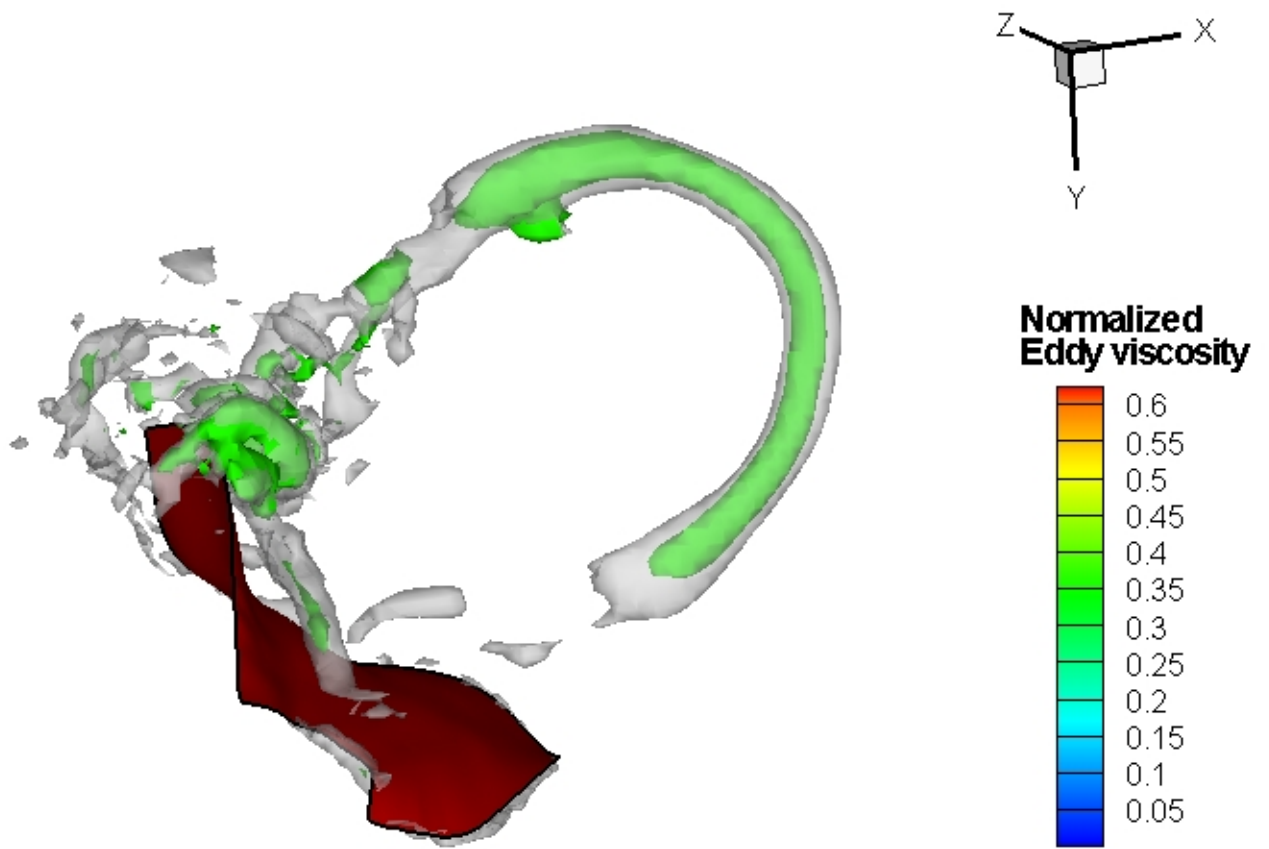


Figure 12. Isosurfaces of eddy viscosity (green) embedded in the vortex structure (gray) of the strongside pectoral fin executing a yaw turn maneuver.